Performance Analysis of Electro-chemical Machining of Ti-48Al-2Nb-2Cr Produced by Electron Beam Melting

Smart and Sustainable Manufacturing Systems

doi:10.1520/SSMS20210041 / Vol. 6 / No. 1 / 2022 / available online at www.astm.org

Manuela Galati,[1] Silvio Defanti,[2] and Lucia Denti[2]

Performance Analysis of Electro-chemical Machining of Ti-48Al-2Nb-2Cr Produced by Electron Beam Melting

Reference

M. Galati, S. Defanti, and L. Denti, "Performance Analysis of Electro-chemical Machining of Ti-48Al-2Nb-2Cr Produced by Electron Beam Melting," *Smart and Sustainable Manufacturing Systems* 6, no. 1 (2022): 53–67. https://doi.org/10.1520/SSMS20210041

ABSTRACT

Ti-48Al-2Nb-2Cr is a challenging and difficult-to-cut titanium aluminide (TiAl) alloy with several manufacturing issues because of the high sensitivity to crack formation and oxygen picking up. Electron beam powder bed fusion (EB-PBF) made feasible TiAl near net shape components, but the surfaces are particularly rough and present complex surface topographies. In this present investigation, experimental analysis and optimization are proposed for electro-chemical machining (ECM) on as-built Ti-48Al-2Nb-2Cr surfaces manufactured using EB-PBF. Experimental runs are performed under pulsed machining conditions and varying specific process metrics to understand the machining effects on the process efficiency and removal phenomena. In particular, the morphology and isotropy of the surface are studied before and after the machining by scanning electron and confocal microscopies. The results establish the optimal machining conditions and a range for the active machining time that produce, compared to the as-built surface, an extremely smooth and isotropy surface without any detrimental effect on the surface integrity and microstructure.

Keywords

roughness, titanium aluminide, electron beam melting, intermetallic, additive manufacturing, surface finishing

Manuscript received October 12, 2021; accepted for publication January 18, 2022; published online February 24, 2022. Issue published February 24, 2022.

[1] Department of Management and Production Engineering, Politecnico di Torino, Corso Duca degli Abruzzi 24, Torino 10129, Italy (Corresponding author), e-mail: manuela.galati@polito.it, https://orcid.org/0000-0001-6508-2594

[2] Department of Engineering, Università di Modena e Reggio Emilia, via P. Vivarelli 10, Modena 41125, Italy, https://orcid.org/0000-0003-4618-3183 (S.D.)

Introduction

Among the powder bed fusion (PBF) additive manufacturing processes, electron beam powder bed fusion (EB-PBF) exploits the power of an electron beam for processing high-melting alloys,[1,2] and also intermetallic materials as γ-TiAl.[3] In particular, titanium aluminide (TiAl) alloys have gained extreme importance in the aerospace industry to

produce aircraft engine parts, where the replacement of nickel-based superalloys opens unique mass saving possibilities[4,5] and a significant reduction of time-to-fly and buy-to-fly ratios.[6,7] Besides the specific properties of strength and Young's modulus, compared to nickel-based superalloys, TiAl shows an excellent creep resistance at an application temperature ranging from 600°C to 800°C.[8] Despite the great industrial interest, its application is limited[9] because the manufacturing of TiAl components is costly and challenging by conventional manufacturing processes. Using a vacuum and hot working environment, EB-PBF makes feasible the production of crack-free components with more homogenous mechanical properties than conventional casting. However, because of the large particle size and hot environment, EB-PBF product shows low surface quality[10] and low dimensional and geometrical accuracy.[11] In addition, owing to the heat transfer mode and the occurrence of sintering phenomena, the EB-PBF surfaces present a complex surface topography characterized by a marked effect of the layer thickness and sintered particles.[10] Because of that, parts produced by the EB-PBF process are still referred to as near net shape, and today a considerable number of post-processing operations based on cutting machining are performed to achieve an acceptable level of finishing. However, high resistance at high temperature and low ductility make TiAl difficult-to-cut materials[12] and more challenging than other titanium alloys.[13] Contact cutting machining of TiAl is unstable because of the rapid and extensive tool wear[14] and the microcrack appearance on the component surface.[15]

In contrast to extensive research on the mechanical and microstructure characterization of TiAl alloys made by EB-PBF,[16] the literature addressing the TiAl machinability is still limited, considering either conventional or nonconventional processes.[4,12,17] The utmost functional advantages of these alloys need to be supported by new research data paving for more easy and efficient finishing options. Rajurkar et al.[18] proposed electro-chemical machining (ECM) as a viable alternative to machine this kind of materials. The main advantage of ECM is the removal method based on a chemical reaction occurring between a cathode tool and the anode workpiece in the presence of an electrolyte solution.[19] Conventional ECM utilizes continuous DC voltage, usually between 6 V and 30 V. The electrolyte fed into the inter-electrode gap (IEG) is, typically, an aqueous solution of NaCl or NaNO3. Besides completing the electrolytic cell, the fluid is necessary to flush away the residues resulting from the ongoing chemical reaction. Pulsed ECM (PECM) is a variation of ECM that allows for a more uniform electric distribution across the gap.[20] Therefore, ECM offers the potential of machining conductive materials without regard to their mechanical properties[21] and tool wear.[18] For instance, Krausset al.[22] successfully machined tungsten, and Mathewet al. [23] used micro ECM to produce tungsten micro tools. Senthilkumar et al.[24] investigated the ECM process of LM25 Al/20%SiC_P composite. Bassu et al.[25] showed the possibility to produce high-complexity microstructures for silicon using micro ECM. Investigating the machined surface of conventionally manufactured titanium, Dhobe et al.[26] showed that high surface quality could be achieved without any thermal effects on the workpiece. They also attempted to produce an engineering surface for the generation of an oxide layer to improve corrosion and chemical resistance under the action of a biofluid. For conventional TiAl, Clifton et al.[27] showed that surfaces with high integrity could be obtained. However, the choice of the electrolyte is critical to avoid surface passivation that occurs with chlorides.

ECM is suitable especially for aerospace applications because the absence of any mechanical contact or thermal effect on the workpiece is highly desirable. The main applications are based on the aerospace industry as a finishing process for turbine blades, including internal channels.[28] However, other applications were also investigated, such as combs for seal elements,[29] gears,[30] molds, and dies, as well as for the production of medical devices and other applications.[31] Additionally, Bao et al.[32] demonstrated the feasibility of ECM for aviation components using pure water as an electrolyte. From an economic point of view, a comparison between ECM, milling, and electro discharge machining showed the feasibility of large production for ECM compared with the other technologies.[33] Klink et al.[34] assessed the technological and economic feasibility of turbocharger impellers by ECM, resulting in a highly efficient result. Norajitra et al.[35] found the ECM for processing tungsten divertor components preferable to the electric discharge machining method, which was time consuming and costly.

For complex topographies such as the one obtained by powder bed fusion (PBF), Defanti et al. showed that, for machining AlSi10Mg parts produced by laser PBF, a pulsed mode is necessary to avoid short-circuiting

because of the release of satellite particles.[36] Their findings also showed a decisive role of fluid dynamics in the gap, in that preexisting pores resulting from laser PBF can cause a local surfeit of material removal.

However, the EB-PBF process differs significantly from the laser PBF because of the vacuum and the hot working environment. Additionally, because of the high sensitivity to crack formation and to microstructure inhomogeneities with respect to other alloys processed by EB-PBF, TiAl is usually processed at extremely high temperatures, using a thicker layer and without contour. These process tricks avoid the temperature drops between one layer and the subsequent and guarantee a uniform temperature and a low cooling rate over the layer and along the build. However, these working conditions contribute to generating unique surface topographies with high surface roughness, which may make challenging the ECM process success and efficiency.

The present article investigates the viability of ECM as a finished process for finishing the high rough parts produced by EB-PBF and made by Ti-48Al-2Nb-2Cr, a γ-TiAl alloy primarily used for the production of low-pressure turbine blades.

Materials and Methods

SPECIMEN PRODUCTION AND ECM

The experiments consisted of producing specimens, in the shape of discs, manufactured in Ti-48Al-2Nb-2Cr by an Arcam A2X, an EB-PBF system, and subsequent finishing by ECM operation. The overall procedure is delineated in the flowchart in **figure 1**, together with the main steps of characterization.

The discs were 5 mm thick, and the diameter was approximately 60 mm. All specimens were built in a single job using Arcam standard Ti-48Al-2Nb-2Cr powder with a size ranging between 45 and 105 μm. The chemical composition is given in **Table 1**. The disks were manufactured with their axis (or the generatrix of the cylinder) perpendicular to the build direction. Solid supports attached the discs to the start plate to ensure a good heat transfer between the specimens and the build platform. The solid support for each specimen consisted of five pillars with a separation width equal to 2 mm. As mentioned above, the parts were processed in a high-temperature environment using a thick layer thickness equal to 1,050°C and 90 μm, respectively. The comprehensive melting process parameter setting consisted of a reference current equal to 10 mA (reference length 25 mm), a focus offset equal to 15 mA, a speed function of 40, and a line offset equal to 0.3 mm. The scanning path was rotated by 90° for every successive layer. The aforementioned parameters would allow to replicate the experiments. The choice of a thick layer and the absence of contouring were expected to give a high roughness of the as-built surfaces. The EBM parameters were constant for all the specimens, in order to achieve a fixed initial condition to be machined with varying ECM parameters.

The finishing operations were carried out using an IMPULSE ECM 50 machine, supplied by pECM System LTD (Yorkshire, UK). The machine works with a maximum voltage of 24V and a maximum current of 1,000A. The system incorporates a numerical control that allows managing the speed and position of the tool. The electrolyte was an aqueous NaCl solution that was selected for the low cost, high safety, and availability. The active end of the tool was a cylinder of CuCrZr alloy. The electrolyte was pumped in the IEG through a specifically designed PLA dispenser to confine and direct the electrolyte flow so that the same electrolytic cell was adopted as in Defanti et al.[36] The density of the electrolyte was maintained at 1.071 g/cm^3 through all the tests. For all the ECM tests, the initial IEG and the flow rate were fixed to 0.5 mm and 3.63 L/min, respectively. ECM was operated in a dynamic mode under pulsed current by varying the following machining parameters: voltage (V), duty cycle (DC), feed rate (f), and machining depth (d). The latter being the final tool position if the zero of coordinates is set on the peaks of the as-built surface, where the tool contacts the surface to be machined. The ECM conditions studied during the experiments are listed in **Table 1**, together with sample nomenclature. The choice of the parameters and of their span was based on previous experience and preliminary tests of ECM finishing of titanium alloys. The following code identifies the specimens: V(V)_DC(%)_f(mm/min) _d(mm). The fourth column in **Table 1** shows the active machining time (AMT), calculated by multiplying the total machining time by the DC. The AMT is the effective time of current flow among the tool and the workpiece when the time-off is subtracted. Based on

FIG. 1 Flowchart of the manufacturing, machining, and characterization steps.

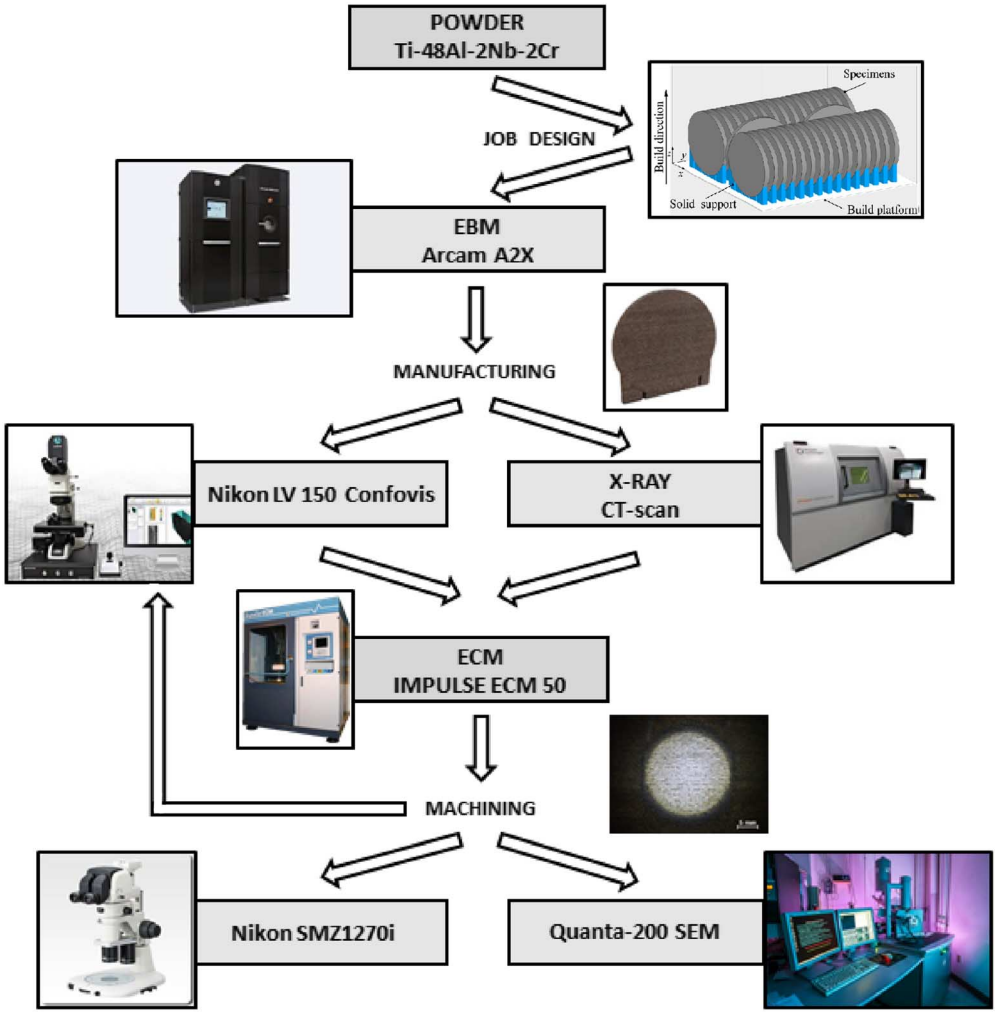

TABLE 1
Sample nomenclature and ECM process parameters

Sample	Voltage, V	Duty Cycle, %	Active Machining Time, s	Feed Rate, mm/min	Machining Depth, mm
20_20_0.5_0	20	20	12	0.5	0
25_30_0.5_0	24	30	18	0.5	0
20_20_0.5_−0.5	20	20	24	0.5	−0.5
24_30_0.5_−0.5	24	30	36	0.5	−0.5
20_40_0.5_−0.5	20	40	48	0.5	−0.5
24_60_0.5_−0.5	24	60	54	0.5	−0.5
20_20_0.5_−1.0	20	20	36	0.5	−1.0
24_30_0.5_−1.0	24	30	48	0.5	−1.0
20_20_0.2_−0.5	20	20	60	0.2	−0.5
24_30_0.2_−0.5	24	30	90	0.2	−0.5

TABLE 2
Chemical compositions of the Ti-48Al-2Nb-2Cr

Factor	Ti	Al	Nb	Cr
Weight, %	Bal	33.4	5.1	2.2
Valence	4	3	0	0

literature studies that showed a beneficial effect of high voltage on TiAl during ECM,[12] the machine was operated at the highest voltage range available to test high values of current density.

A preliminary test was conducted in continuous mode, with a voltage equal to 24V and the final height set at −0.5 mm. This test was meant to measure the current flowing in the electrolytic cell.

The theoretical material removal rate (MRR), expressed in grams per minute, was calculated by applying Faraday's equation for a metal alloy according to equation (1):

$$\mathrm{MRR} = \frac{m}{t} = \frac{I}{F\sum_i \frac{x_i Z_i}{A_i}} \tag{1}$$

where m is the removed mass, expressed in grams; I is the current, expressed in amperes; t is the total machining time in minutes; x_i, Z_i, and A_i are the weight fraction, the valence, and the atomic weight (expressed in g/mol) of the element ith element according to Table 2, respectively; F is the Faraday's constant and was set equal to 96.485 C/mol.

In order to estimate the productivity under each machining condition, the value for t used to compute the MRR was the total duration of the ECM process, i.e., the AMT divided by the DC.

CHARACTERIZATION

A representative specimen porosity and distribution of pores were investigated by an X-ray computed tomography scanner (CT-scan) (GE Phoenix v|tome|x s). The scans were performed using a voltage of 235 kV, a current of 110 μA, and 0.5-mm-thick copper filter. In order to achieve a higher resolution, a region of interest (ROI) was selected for the scanning. Therefore, the selected voxel size was 0.025 mm, equal to about one-fourth of the layer thickness and smaller than the smallest powder particle dimensions. The ROI also included a portion close to the solid support. The post-processing of the acquired CT projections was performed using VGStudioMax 3.4. With the same software, the three-dimensional (3D) volume was reconstructed, and the porosity analysis was carried out with the integrated tool after the definition of the external surface of the scanned ROI. The external surface was determined using the average material grey and average background grey values.

Each sample was inspected through the Nikon SMZ1270i Stereo Microscope (Nikon, Japan). The roughness of all the as-built samples and the corresponding EC machined surfaces was ascertained according to ISO 25178-2.[37] The surface topography was analyzed using a Nikon LV 150 Confovis Microscope under the setup described as follows: 100x microscopic objective; scanned area of 2.42 mm by 1.72 mm obtained by stitching 3 by 2 scan patches acquired using the double exposure method. After form removal, maps were processed by a FALS filter, according to Rajurkar et al.,[18] with a cut-off of 0.008 μm and 0.1–99.9 % bilateral symmetric threshold filtering (for removing spikes). The resulting maps were then scrutinized to confirm surface homogeneity and used to extract the 3D average areal surface roughness (Sa).

Moreover, reduced peak (Spk) and valley (Svk) height were determined, as well as skewness (Ssk) and kurtosis (Sku). Owing to the heterogeneity of the as-built sample, the machining effectiveness was evaluated by comparing one-to-one the surface morphology before and after the ECM finishing. As prescribed in ISO 25178-2:2012,[37] the surface characterization was strengthened by calculating the texture aspect ratio (Str) and the texture direction (Std), as in Denti and Sola.[38] Str ranges between 0 and 1, where zero indicates high

TABLE 3
Key Performance Indicators and methods used for their assessment

Key Perfomance Indicators	Measuring Method
Reduction of Sa	Confocal microscopy
Reduction of Spk	Confocal microscopy
Reduction of Svk	Confocal microscopy
Increase in Str (closer to 1)	Confocal microscopy
High MRR	Calibrated optical and confocal microscopy
Surface homogeneity	SEM observation
Absence of intergranular corrosion	SEM observation
Absence of intergranular corrosion	Optical microscopy of etched sections
SEM observation	

anisotropy and 1 signifies high isotropic surface texture. Std represents the lay of the surface features. The specimens were positioned so that, in the polar spectrum, the angle 0°/180° is parallel to the layers and orthogonal to the build direction.

The sample surface morphology of each specimen was observed inspected by using a scanning electron microscope (SEM; Quanta-200, Fei Company, Oxford Instruments, UK) to investigate the removal phenomena.

The experimental MRR was determined as the product of the machined volume times the material density, measured using the Archimedes method and equal to 4.071 g/cm^3. The machined volume was quantified via calibrated optical images and confocal microscopy to measure the diameter and depth of the eroded zone.

Each sample was cut along a plane perpendicular to the ECMed surface and aligned to the build direction for the EB-PBF process. Polished sections were observed using a Nikon SMZ1270i microscope, and measurements on the peaks and valleys were collected on the calibrated images. Furthermore, the specimen sections were etched using a solution of Kroll (6 vol.% nitric acid and 3 vol.% hydrofluoric acid in water), and the surface was photographed with the Nikon SMZ1270i.

A summary of the metrics of performance that have been used for the assessment of the results and the methods by which they were measured is provided in Table 3.

Results and Discussion

Figure 2 shows the 3D reconstructed geometry of a portion of the sample acquired by X-ray CT scanning. The sample surfaces are characterized by the typical ripples along the build direction (fig. 2*A*) because of the absence of contour melting strategy and the thick layer thickness. The ripples are blurred closer to the support structure and become well defined along the build direction (fig. 2*B*). The as-built specimen morphology can also be well appreciated through the polished cross-section of the sample (fig. 3*A*), where peaks as high as 200 μm and deep valleys (400–500 μm) were spotted. The build direction during the EB-PBF process was vertical in the image, as in all the polished sections shown for the machined specimens. Cracks aligned to the layers generated by the high

FIG. 2
X-ray CT analysis of the as-built surface: (*A*) cross section of the sample and (*B*) 3D surface reconstruction.

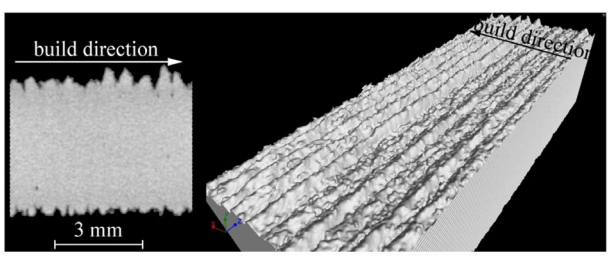

(*A*) (*B*)

FIG. 3 As-built sample: (*A*) cross section and (*B*) 3D surface map.

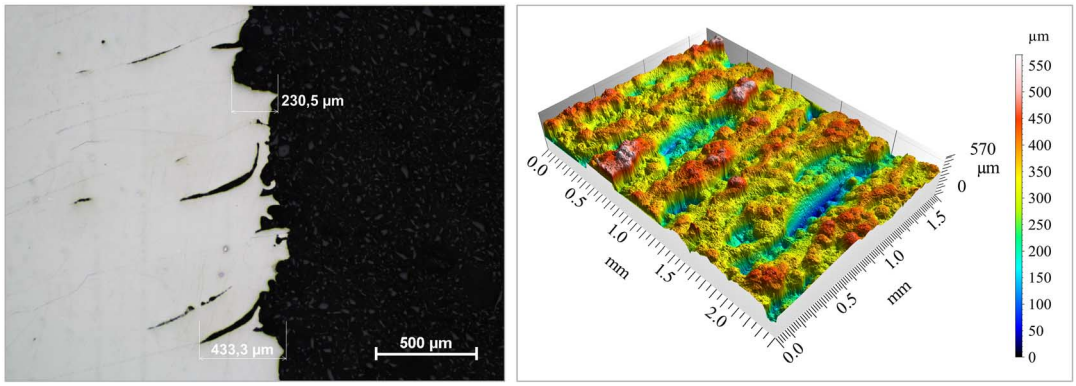

(*A*) (*B*)

thermal gradient between the melted material and surroundings are visible close to the external surfaces during the EB-PBF process. The complexity of the surface topography was depicted in **figure 3*B***, in which it is possible to observe sintered or partially melted and deep valleys.

The porosity analysis showed low pores (**fig. 4**) and a defect volume ratio of 0.26 %, corresponding to a relative density value equal to 99.74 %. Large pores with an irregular shape were detected (**fig. 4*A***). However, the presence of these pores is localized at the boundary between the bulk material and the support structure, where the transition area causes low thermal stability. Most of the pores (**fig. 3*B***) have a small dimension (lower than 0.4 mm) and a high sphericity index (higher than 0.6), which indicates a nearly spherical shape of the pores.

A current between 100 A and 112 A flowing through the electrolytic cell was selected from the preliminary test conducted in continuous mode. The complete set of results is collected in **Table 4**, where the surface parameters are collected for each specimen in the as-built (AB) and machined (Mach.) conditions. Percent reductions are computed for the quantitative parameters Sa, Spk, and Svk, whereas the descriptive metrics Ssk, Sku, Str, and Std are displayed for the qualification of the surface morphology. **Figures 5** and **6** collect the cross-section and surface topography for each machined sample.

FIG. 4 X-ray CT analysis of the as-built sample: (*A*) porosity analysis and (*B*) sphericity index.

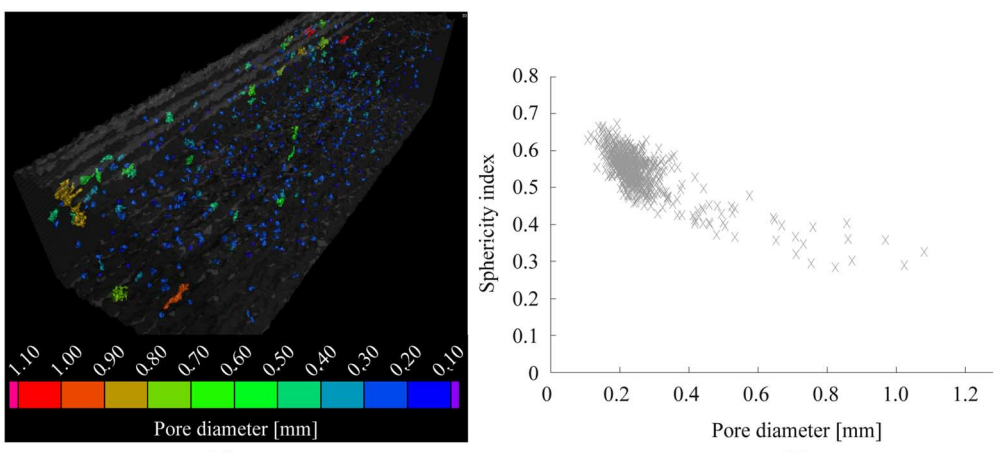

(*A*) (*B*)

TABLE 4

MRR and the surface parameters for each sample in the as-built (AB) and machined (Mach.) conditions

MRR and the Surface Parameters	Material Conditions and Comparison	20_20_0.5_0	24_30_0.5_0	20_20_0.5_−0.5	24_30_0.5_−0.5	20_40_0.5_−0.5	24_60_0.5_−0.5	20_20_0.5_−1.0	24_30_0.5_−1.0	20_20_0.2_−0.5	24_30_0.2_−0.5
MRR mg/min		3.25	3.86	2.2	1.93	3.52	5.95	1.41	…	1.48	1.85
Sa, μm	AB	58.7	57.1	58.9	80.1	59	65.7	65.8	…	64.1	62.9
	Mach.	29.4	29.3	24.6	17.8	12.8	5.1	13.5	…	9.9	6
	Reduction, %	50	49	58	78	78	92	79	…	85	90
Ssk	AB	0.021	−0.609	−0.456	−0.387	0.101	0.744	−0.456	…	0.214	−0.717
	Mach.	−0.245	−0.445	−1.34	−0.173	0.11	−0.007	−1.34	…	−0.041	−0.149
Sku	AB	2.65	3.6	3.44	2.66	2.88	3.94	3.44	…	3.47	3.84
	Mach.	3.06	3.1	5.07	3.18	3.54	5.04	5.07	…	2.78	3.24
Spk, μm	AB	66	53.4	56.8	52.8	56.5	60.4	56.8	…	86.6	44.7
	Mach.	23.5	18.3	8.03	19.7	18.1	6.3	8	…	12.1	6.2
	Reduction, %	64	66	86	63	68	90	86	…	86	86
Svk, μm	AB	59.1	109	98.2	112	87	136	98.2	…	75.5	113
	Mach.	41.3	44.1	61.4	26.4	15.8	7.3	61.4	…	10.3	7.9
	Reduction, %	30	60	37	76	82	95	37	…	86	93
Str	AB	0.241	0.260	0.341	0.175	0.194	0.111	0.139	…	0.099	0.445
	Mach.	0.230	0.217	0.122	0.356	0.260	0.394	0.405	…	0.197	0.709
Std	AB	174	175	6	175	4	4	6	…	177	29
	Mach.	4	177	176	3	3	177	3	…	177	172

FIG. 5 Sections of ECMed samples: (*A*) 20_20_0.5_–0.5, (*B*) 24_30_0.5_–0.5, (*C*) 20_40_0.5_–0.5, (*D*) 24_60_0.5_–0.5, (*E*) 20_20_0.5_0, (*F*) 24_30_0.5_0, (*G*) 20_20_0.2_–0.5, and (*H*) 24_30_0.2_–0.5.

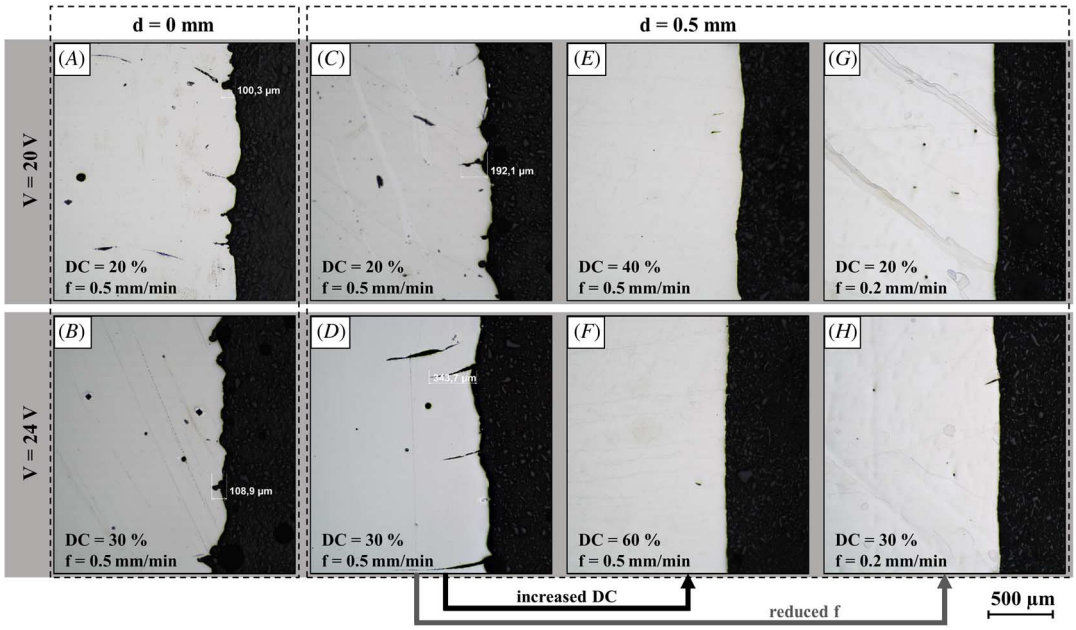

FIG. 6 The 3D surface maps of the ECMed samples: (*A*) 20_20_0.5_–0.5, (*B*) 24_30_0.5_–0.5, (*C*) 20_40_0.5_–0.5, (*D*) 24_60_0.5_–0.5, (*E*) 20_20_0.5_0, (*F*) 24_30_0.5_0, (*G*) 20_20_0.2_–0.5, and (*H*) 24_30_0.2_–0.5.

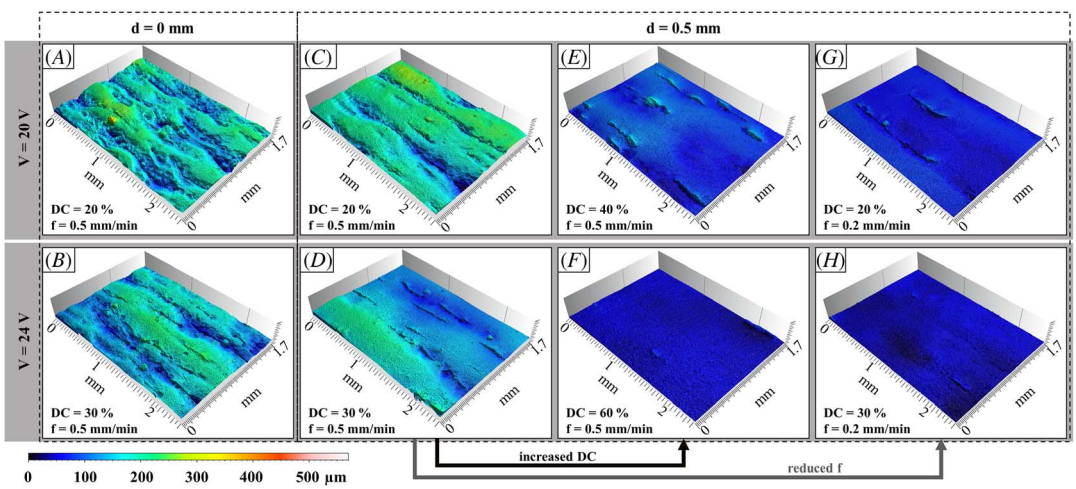

The comparison by one-to-one sample showed the following results. For all samples, the surface roughness was decreased to a great extent by the EC machining. For d equal to zero, the ECM finishing provides a reduction of Sa of 50 % and 49 % for the samples 20_20_0.5_0 and 24_30_0.5_0, respectively. The corresponding section (**fig. 5*A*** and **5*B***) shows that, despite a consistent roughness decrease, the machining of peaks is almost complete, whereas valleys are still noticeable. **Figure 6*A*** and **6*B*** show that the surface topographies confirm that finding, partially described by the Spk and Svk values. In fact, the peak reduction percentage (**Table 3**) is 64 % for

specimen 20_20_0.5_0 and 66 % for specimen 24_30_0.5_0, whereas the valleys show a reduction of only 30 % and 60 % for the specimens 20_20_0.5_0 and 24_30_0.5_0, respectively. However, it should be considered that confocal microscopy is likely to underestimate the depth of valleys, as in the case of narrow and deep cracks, the measurement can lose efficacy.

An increasing d up to 0.5 mm below the surface of the as-built workpiece showed improved efficacy of the finishing process (Table 3). Sections of the samples 20_20_0.5_−0.5 and 24_30_0.5_−0.5 are shown in figure 5*B* and 5*C*, and the surface maps in figure 6*C* and 6*D*, respectively. In particular, for the sample machined with a voltage and a DC equal to 24V and 30 %, respectively, the Sa reduction is remarkable (78 %). The section and the surface map revealed a further machining progression with respect to the corresponding counterpart stopped at $d = 0$ mm.

The samples 20_20_0.5_−1.0 and 24_30_0.5_−1.0 exploited an even increased d. Owing to the extended tool path, the IEG for the latter test clogged. For this reason, the test was aborted. However, the first test was conducted entirely and provided an Sa reduction similar to that counterpart machined with $d = -0.5$ mm. The test 20_20_0.5_−1.0 was not included in figures 5 and 6 because of the short-circuiting problems.

Increased DC (samples 20_40_0.5_−0.5 and 24_60_0.5_−0.5) showed an impressive Sa reduction from 78 to 92 % (Table 4). Moreover, the Spk and Svk values (Table 4) show the machining effectiveness in reducing the valleys and the peaks. The sections reported in figure 5*E* and 5*F* and the maps in figure 6*E* and 6*F* confirm that these ECM conditions provide a planar surface without peaks or valleys.

A lower f than 0.5 mm/min, corresponding to the samples 20_20_0.2_−0.5 and 24_30_0.2_−0.5, verified if the results with a higher DC were comparable to those with a lower speed, as both involve high values of AMT. The sections of these specimens are represented in figure 5*G* and 5*H*. Similarly to what was attained with higher DC, the lower f reduced Sa by approximately 84 % and 90 % (Table 4), and peaks and valleys underwent a similar diminishing.

Figure 7 reports SEM images of specimen 24_60_0.5_−0.5, in which three different zones can be distinguished: (A) the finished surface, (B) the transition surface between the machined and the not machined (as-built) surfaces, and (C) the not machined surfaces (as-built). The as-built surfaces (fig. 7*C*) show satellite particles presence and the unevenness related to the layer overlapping. Figure 6*A* and 6*B* allow appreciation of the progressive erosion phenomena. The material removal begins with the satellite particles detachment, proceeds with the peaks dissolution, and continues with a surface flattening. However, because of the initial morphology produced by EB-PBF and to the memory effect amplified by fluid dynamic occurrences, in agreement with Defanti et al.,[36] valleys are sometimes reproduced at a lower depth or turn into "canyons" eroded into the specimen (fig. 6*A*). The result is confirmed by the measurements taken on the calibrated images of the group of samples corresponding to figure 4*A*–4*D*, where the depth of valleys is in some cases maintained even for a d value that is nominally sufficient to erase the valleys that were present on the as-built specimens completely. It can be reckoned that, in all the tests with an AMT shorter than 40 s, the ECM process was stopped too early and was insufficient to flatten the initial morphology. Good results are initially obtained with the erosion of peaks,

FIG. 7

SEM image of the specimen 24_60_0.5_−0.5: (*A*) ECMed surface with a "canyon" highlighted by the dotted line; (*B*) AB-ECMed transition zone; (*C*) AB zone.

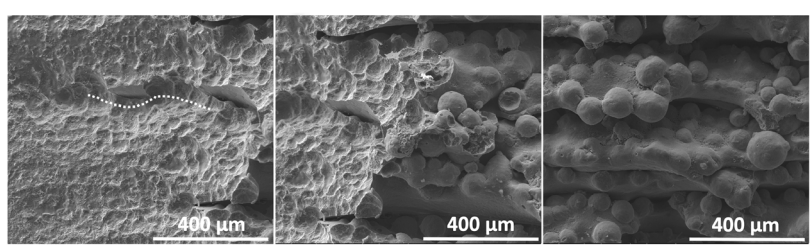

FIG. 8

Sample 24_60_0.5_−0.5: (*A*) central area; (*B*) detail of a residual crest.

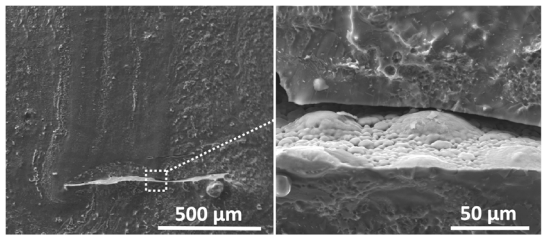

whereas valleys require further machining. Above that AMT threshold, both a DC increase and an f reduction allowed the achievement of smooth surfaces. Deeper machining is not viable because of incorrect electrolyte flow through the IEG, insufficient debris removal, and short-circuiting. The result is that peaks are efficiently removed at the commencing of the ECM process, but the erosion then stops prematurely.

In the best cases, as for sample 24_60_0.5_−0.5, the central area of the machined surface is exceptionally smooth, with some local morphological variations because of the electrolyte flow (**fig. 8*A***). The result agrees with previous studies reported by Defanti et al.[36] on AlSi10Mg produced by L-PBF and Kozak and Zybura-Skrabalak,[39] where the flow field in the gap can cause a localized surplus of dissolution. In the present research, differently from Kozak and Zybura-Skrabalak,[39] the local increase of the electrolyte speed does not produce ripples but turns instead into an additional surface smoothing effect. The different outcome is likely to be ascribed to the high hardness of TiAl. The magnification in **figure 8*B*** allows appreciating a detail of one of the crests that remain on the generally smooth surface. These edges derive from defects generated during the EB-PBF process because the inner surface of the defect shows the morphology typically obtained during solidification. Because of the flow field, the upstream region suffers from insufficient machining, whereas the erosion is more pronounced downstream.

Figure 9 shows a visual portrayal of the effect of the ECM process on the bearing area using the Abbott-Firestone curve of sample 24_60_0.5_−0.5 compared with the corresponding as-built counterpart. An additional effect of the ECM process is the anisotropy reduction as the EB-PBF as-built parts. In general, the anisotropy of the AB surfaces was reduced after machining, to a great extent that is quantified by the Str increase (**Table 4**) that, in the best cases, is impressive and equal to 200–250 %. The first dominant surface direction calculated using the Fourier transform is around 0°/180° for all the specimens, before and after ECM, but the isotropy of the surfaces was significantly enhanced after machining. **Figure 10** shows an example of a polar plot of texture direction for the AB surface and the machined counterpart, in which no privileged direction of surface structure can be observed. The result is totally analogous for sample 24_60_0.5_−0.5.

Figure 11 shows the etched sections of sample 20_20_0.2_−0.5 and corresponding AB. Specimen 24_60_0.5_−0.5 shows the same result. The grain structure obtained by EB-PBF is not affected by the ECM process. The

FIG. 9

Abbott-Firestone curve of sample 24_60_0.5_−0.5 as compared with an AB surface.

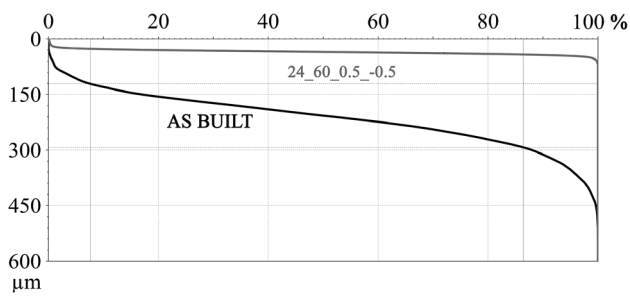

FIG. 10 Polar plot of texture direction for the specimen 24_30_0.2_–0.5: AB (*A*) and machined (*B*).

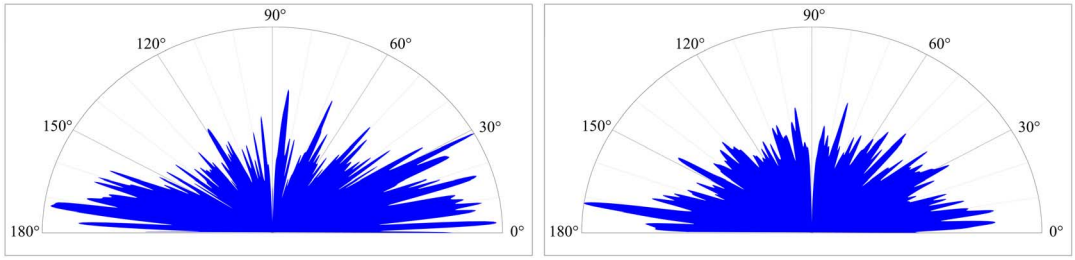

FIG. 11 Etched sections of sample 20_20_0.2_–0.5: AB (*A*) and machined (*B*).

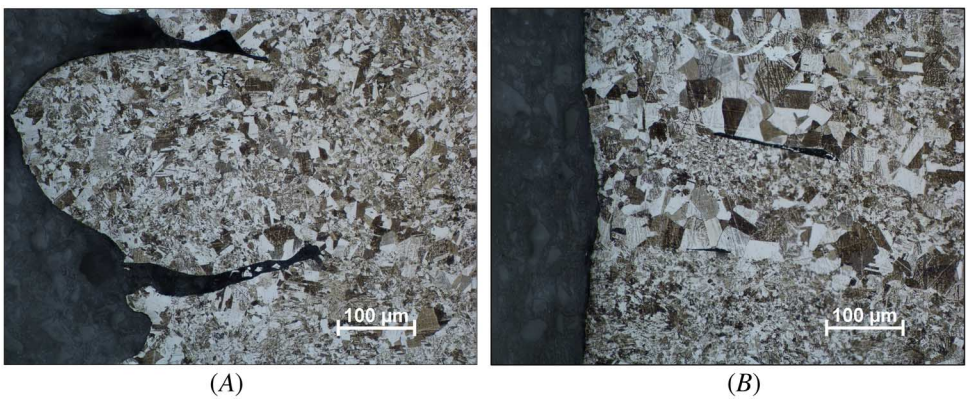

unvaried microstructure confirmed the finding reported by Klocke et al.[40] and the definition of ECM as a "cold" technology that does not generate any thermal and local microstructure modifications. Contrary to previous ECM studies addressing other metals, such as aluminum alloys,[36] no intergranular corrosion was observed in the SEM images or the etched sections. The absence of intergranular corrosion for TiAl ECMed in a NaCl environment is consistent with previous findings available in the literature.[41]

Figure 12 plots the effect of MRR and the AMT on the Sa values to present an overall perspective of the process performances in the experimental domain considered in this research. Figure 12*A* shows that low surface

FIG. 12 (*A*) Plot of Sa versus MRR; (*B*) plot of Sa versus AMT.

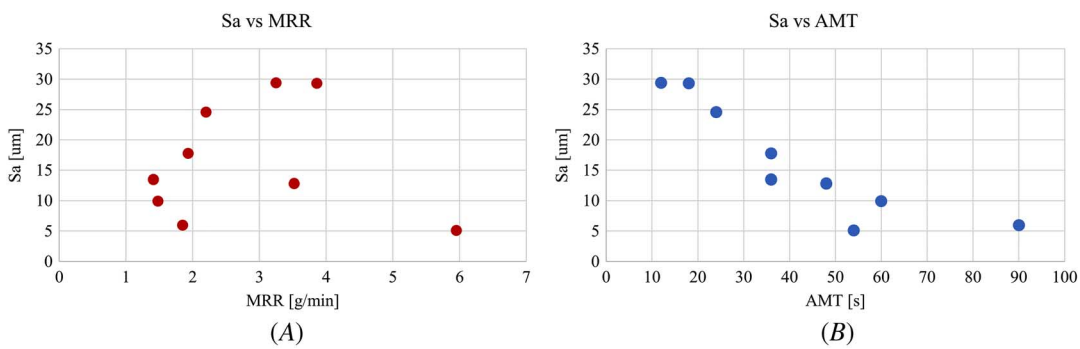

roughness values are generally associated with machining conditions characterized by low MRR. An extremely interesting exception can be spotted for test 24_60_0.5_−0.5, which provided the highest MRR together with one of the smoothest surfaces. The best results with regard to the surface finish were achieved for the samples 24_60_0.5_−0.5 and 24_30_0.2_−0.5, with comparable values of areal surface roughness cut down to 5–6 μm, and a highly effective flattening of peaks and removal of valleys. Nevertheless, it is worth remarking that the two machining conditions provide significantly different values of MRR. The test 24_60_0.5_−0.5 benefits more than three times higher productivity for equally smooth finished surfaces than for the test with a reduced f. In the considered conditions, a DC of 60 % is not too high to hamper the flushing of the machining residues if the d does not exceed −0.5mm. The plot in **figure 12*B*** shows that a strong relationship might be established between Sa and AMT: surface roughness decreases quite regularly by increasing AMT. This finding is well in agreement with some work in the literature.[42] Similar values of MRR were measured also measured by Klocke et al.[40] However, it is impossible to compare the surface roughness values because they polished the specimens before the ECM process to eliminate the initial surface morphology.[40] A final remark in the discussion should be dedicated to the geometry of the EC machined surfaces. The findings are promising for a relatively smooth extension of the feasibility of ECM for the finishing of curved or generally more complex surfaces, on condition that the dielectric dispenser is designed so that to ensure a proper electrolyte flow through the IEG.

Conclusions

TiAl was successfully machined by ECM, with a surface roughness reduction of approximately 90 % in the best case. With respect to the parameter space that was used for experimenting, the optimal machining conditions were found to be a voltage of 24V, a d of 0.5 mm below the as-built surface, and an AMT between the 50s and 90s, achieved by acting on the DC or f. Higher machining depths produced or short-circuiting problems or a negligible process efficiency enhancement.

Extremely high productivity was accomplished using a DC and a f of 60 % of 0.05 mm/min, respectively, without any detrimental effect on the surface integrity. ECM effectively reduced the anisotropy of the layered surfaces while keeping the grain structure unaltered and without causing any intergranular corrosion. The key advantage of a solution that combines EBM and ECM is the overcoming of the manufacturing difficulties that hamper a quicker diffusion of TiAl. The findings corroborate the hypothesis that the flow field in the gap, in the presence of geometrical unevenness, is decisive on the onset of enhanced erosion phenomena. The local increase of the electrolyte speed does not produce ripples but turns instead into an additional surface smoothing effect. A limitation of ECM finishing of EBM-made parts is the use of a dedicated tool, whereas tool-less processes benefit from a more straightforward application. Developments of this research are tackling innovative tooling options to strengthen the impact of the current results.

References

1. C. Körner, H. Helmer, A. Bauereiß, and R. F. Singer, "Tailoring the Grain Structure of IN718 during Selective Electron Beam Melting," *MATEC Web of Conferences* 14 (2014): 08001, https://doi.org/10.1051/matecconf/20141408001
2. V. V. Popov, M. L. Grilli, A. Koptyug, L. Jaworska, A. Katz-Demyanetz, D. Klobčar, S. Balos, B. O. Postolnyi, and S. Goel, "Powder Bed Fusion Additive Manufacturing Using Critical Raw Materials: A Review," *Materials* 14, no. 4 (February 2021): 909, https://doi.org/10.3390/ma14040909
3. C. Körner, "Additive Manufacturing of Metallic Components by Selective Electron Beam Melting—A Review," *International Materials Reviews* 61, no. 5 (July 2016): 361–377, https://doi.org/10.1080/09506608.2016.1176289
4. S. Biamino, A. Penna, U. Ackelid, S. Sabbadini, O. Tassa, P. Fino, M. Pavese, P. Gennaro, and C. Badini, "Electron Beam Melting of Ti-48Al-2Cr-2Nb Alloy: Microstructure and Mechanical Properties Investigation," *Intermetallics* 19, no. 6 (June 2011): 776–781, https://doi.org/10.1016/j.intermet.2010.11.017
5. A. Katz-Demyanetz, V. V. Popov, A. Kovalevsky, D. Safranchik, and A. Koptyug, "Powder-Bed Additive Manufacturing for Aerospace Application: Techniques, Metallic and Metal/Ceramic Composite Materials and Trends," *Manufacturing Review* 6 (March 2019): 5, https://doi.org/10.1051/mfreview/2019003

6. V. Petrovic and R. Niñerola, "Powder Recyclability in Electron Beam Melting for Aeronautical Use," *Aircraft Engineering and Aerospace Technology* 87, no. 2 (March 2015): 147–155, https://doi.org/10.1108/AEAT-11-2013-0212
7. B. Lin, W. Chen, Y. Yang, F. Wu, and Z. Li, "Anisotropy of Microstructure and Tensile Properties of Ti–48Al–2Cr–2Nb Fabricated by Electron Beam Melting," *Journal of Alloys and Compounds* 830 (July 2020): 154684, https://doi.org/10.1016/j.jallcom.2020.154684
8. L. E. Murr, S. M. Gaytan, A. Ceylan, E. Martinez, D. H. Hernandez, B. I. Machado, D. A. Ramirez, et al., "Characterization of Titanium Aluminide Alloy Components Fabricated by Additive Manufacturing Using Electron Beam Melting," *Acta Materialia* 58, no. 5 (March 2010): 1887–1894, https://doi.org/10.1016/j.actamat.2009.11.032
9. V. Güther, M. Allen, J. Klose, and H. Clemens, "Metallurgical Processing of Titanium Aluminides on Industrial Scale," *Intermetallics* 103 (December 2018): 12–22, https://doi.org/10.1016/j.intermet.2018.09.006
10. M. Galati, G. Rizza, S. Defanti, and L. Denti, "Surface Roughness Prediction Model for Electron Beam Melting (EBM) Processing Ti6Al4V," *Precision Engineering* 69 (May 2021): 19–28, https://doi.org/10.1016/j.precisioneng.2021.01.002
11. P. Minetola, M. Galati, F. Calignano, L. Iuliano, G. Rizza, and L. Fontana, "Comparison of Dimensional Tolerance Grades for Metal AM Processes," *Procedia CIRP* 88 (January 2020): 399–404, https://doi.org/10.1016/j.procir.2020.05.069
12. D. K. Aspinwall, R. C. Dewes, and A. L. Mantle, "The Machining of γ-TiAl Intermetallic Alloys," *CIRP Annals* 54, no. 1 (January 2005): 99–104, https://doi.org/10.1016/S0007-8506(07)60059-6
13. M. Rahman, Y. S. Wong, and A. R. Zareena, "Machinability of Titanium Alloys," *JSME International Journal Series C Mechanical Systems, Machine Elements and Manufacturing* 46, no. 1 (2003): 107–115, https://doi.org/10.1299/jsmec.46.107
14. A. R. C. Sharman, D. K. Aspinwall, R. C. Dewes, D. Clifton, and P. Bowen, "The Effects of Machined Workpiece Surface Integrity on the Fatigue Life of γ-Titanium Aluminide," *International Journal of Machine Tools and Manufacturing* 41, no. 11 (September 2001): 1681–1685, https://doi.org/10.1016/S0890-6955(01)00034-7
15. E. Uhlmann, G. Frommeyer, S. Herter, S. Knippscheer, and J. M. Lischka, "Studies on the Conventional Machining of TiAI-Based Alloys," in *Ti-2003 Science and Technology, Volume I: Proceedings of the 10th World Conference on Titanium* (Weinheim, Germany: Wiley-VCH, 2003): 2293–2300.
16. M. Galati and L. Iuliano, "A Literature Review of Powder-Based Electron Beam Melting Focusing on Numerical Simulations," *Additive Manufacturing* 19, no. 1 (January 2018): 1–20, https://doi.org/10.1016/j.addma.2017.11.001
17. G. Baudana, S. Biamino, D. Ugues, M. Lombardi, P. Fino, M. Pavese, and C. Badini, "Titanium Aluminides for Aerospace and Automotive Applications Processed by Electron Beam Melting: Contribution of Politecnico di Torino," *Metal Powder Report* 71, no. 3 (May 2016): 193–199, https://doi.org/10.1016/j.mprp.2016.02.058
18. K. P. Rajurkar, M. M. Sundaram, and A. P. Malshe, "Review of Electrochemical and Electrodischarge Machining," *Procedia CIRP* 6 (January 2013): 13–26, https://doi.org/10.1016/j.procir.2013.03.002
19. K. P. Rajurkar, J. Kozak, B. Wei, and J. A. McGeough, "Study of Pulse Electrochemical Machining Characteristics," *CIRP Annals* 42, no. 1 (January 1993): 231–234, https://doi.org/10.1016/S0007-8506(07)62432-9
20. J. J. J. Wang, C. K. Chung, B. H. Wu, and Y. Y. Liao, "Fabrication of Wedge-Shape Tool via Electrochemical Micromachining with Diamond-Like Carbon Coating," *Journal of Materials Processing Technology* 187–188 (June 2007): 264–269, https://doi.org/10.1016/j.jmatprotec.2006.11.069
21. B. Walther, J. Schilm, A. Michaelis, and M. M. Lohrengel, "Electrochemical Dissolution of Hard Metal Alloys," *Electrochimica Acta* 52, no. 27 (October 2007): 7732–7737, https://doi.org/10.1016/j.electacta.2006.12.038
22. W. Krauss, N. Holstein, and J. Konys, "Advanced Electro-chemical Processing of Tungsten Components for He-Cooled Divertor Application," *Fusion Engineering and Design* 85, nos. 10–12 (December 2010): 2257–2262, https://doi.org/10.1016/j.fusengdes.2010.09.005
23. R. Mathew and M. M. Sundaram, "Modeling and Fabrication of Micro Tools by Pulsed Electrochemical Machining," *Journal of Materials Processing Technology* 212, no. 7 (July 2012): 1567–1572, https://doi.org/10.1016/j.jmatprotec.2012.03.004
24. C. Senthilkumar, G. Ganesan, R. Karthikeyan, and S. Srikanth, "Modelling and Analysis of Electrochemical Machining of Cast Al/20%SiCp Composites," *Materials Science and Technology* 26, no. 3 (March 2010): 289–296, https://doi.org/10.1179/174328409X459239
25. M. Bassu, S. Surdo, L. M. Strambini, and G. Barillaro, "Electrochemical Micromachining as an Enabling Technology for Advanced Silicon Microstructuring," *Advanced Functional Materials* 22, no. 6 (January 2012): 1222–1228, https://doi.org/10.1002/adfm.201102124
26. S. D. Dhobe, B. Doloi, and B. Bhattacharyya, "Analysis of Surface Characteristics of Titanium during ECM," *International Journal of Machining and Machinability of Materials* 10, no. 4 (October 2011): 293–309, https://doi.org/10.1504/IJMMM.2011.043085
27. D. Clifton, A. R. Mount, D. J. Jardine, and R. Roth, "Electrochemical Machining of Gamma Titanium Aluminide Intermetallics," *Journal of Materials Processing Technology* 108, no. 3 (January 2001): 338–348, https://doi.org/10.1016/S0924-0136(00)00739-1
28. J. Pattavanitch and S. Hinduja, "Machining of Turbulated Cooling Channel Holes in Turbine Blades," *CIRP Annals* 61, no. 1 (January 2012): 199–202, https://doi.org/10.1016/j.cirp.2012.03.086
29. S. P. Pavlinich, A. R. Mannapov, N. Z. Gimaev, and A. N. Zaitsev, "Electrochemical Shaping of Aerodynamic Seal Elements," *Russian Aeronautics* 51, no. 3 (October 2008): 330–338, https://doi.org/10.3103/S1068799808030161
30. L. Huang, Y. Cao, F. Jia, and Y. Lei, "Research on Spur Face Gear by Electrochemical Machining Based on the Complex Surface Mesh," *Chaos, Solitons and Fractals* 130 (January 2020): 109443, https://doi.org/10.1016/j.chaos.2019.109443

31. A. Zabel and M. Heilmann, "Deep Hole Drilling Using Tools with Small Diameters—Process Analysis and Process Design," *CIRP Annals* 61, no. 1 (January 2012): 111–114, https://doi.org/10.1016/j.cirp.2012.03.002
32. H. Bao, J. Xu, and Y. Li, "Aviation-Oriented Micromachining Technology—Micro-ECM in Pure Water," *Chinese Journal of Aeronautics* 21, no. 5 (October 2008): 455–461, https://doi.org/10.1016/S1000-9361(08)60059-X
33. F. Klocke, M. Zeis, A. Klink, and D. Veselovac, "Technological and Economical Comparison of Roughing Strategies via Milling, Sinking-EDM, Wire-EDM and ECM for Titanium- and Nickel-Based Blisks," *CIRP Journal of Manufacturing Science and Technology* 6, no. 3 (January 2013): 198–203, https://doi.org/10.1016/j.cirpj.2013.02.008
34. A. Klink, M. Hlavac, T. Herrig, and M. Holsten, "Technological and Economical Assessment of Alternative Process Chains for Turbocharger Impeller Manufacture," *Procedia CIRP* 77 (January 2018): 586–589, https://doi.org/10.1016/j.procir.2018.08.212
35. P. Norajitra, L. V. Boccaccinia, A. Gervash, R. Giniyatulin, N. Holstein, T. Ihli, G. Janeschitz, et al., "Development of a Helium-Cooled Divertor: Material Choice and Technological Studies," *Journal of Nuclear Materials* 367–370 (August 2007): 1416–1421, https://doi.org/10.1016/j.jnucmat.2007.04.027
36. S. Defanti, L. Denti, N. Vincenzi, and A. Gatto, "Preliminary Assessment of Electro-chemical Machining for Aluminum Parts Produced by Laser-Based Powder Bed Fusion," *Smart Sustainable Manufacturing Systems* 4, no. 1 (November 2020): 121–134, https://doi.org/10.1520/SSMS20200039
37. *Geometrical Product Specifications (GPS)—Surface Texture: Areal—Part 2: Terms, Definitions and Surface Texture Parameters*, ISO 25178-2 (2012) (Geneva, Switzerland: International Organisation of Standardization).
38. L. Denti and A. Sola, "On the Effectiveness of Different Surface Finishing Techniques on A357.0 Parts Produced by Laser-Based Powder Bed Fusion: Surface Roughness and Fatigue Strength," *Metals* 9, no. 12 (November 2019): https://doi.org/10.3390/met9121284
39. J. Kozak and M. Zybura-Skrabalak, "Some Problems of Surface Roughness in Electrochemical Machining (ECM)," *Procedia CIRP* 42 (January 2016): 101–106, https://doi.org/10.1016/j.procir.2016.02.198
40. F. Klocke, T. Herrig, M. Zeis, and A. Klink, "Comparison of the Electrochemical Machinability of Electron Beam Melted and Casted Gamma Titanium Aluminide TNB-V5," *Proceedings of the Institution of Mechanical Engineers, Part B: Journal of Engineering Manufacture* 232, no. 4 (March 2018): 586–592, https://doi.org/10.1177/0954405416687147
41. A. Mohammad, A. M. Al-Ahmari, V. K. Balla, M. Das, S. Datta, D. Yadav, and G. D. Janaki Ram, "In Vitro Wear, Corrosion and Biocompatibility of Electron Beam Melted γ-TiAl," *Materials & Design* 133 (November 2017): 186–194, https://doi.org/10.1016/j.matdes.2017.07.065
42. X. Chen, Z. Xu, D. Zhu, Z. Fang, and D. Zhu, "Experimental Research on Electrochemical Machining of Titanium Alloy Ti60 for a Blisk," *Chinese Journal of Aeronautics* 29, no. 1 (February 2016): 274–282, https://doi.org/10.1016/j.cja.2015.09.010